
Volume 98, Issue 12, December 2010
ISSN 0167-6105
ELSEVIER
Journal of
Wind Engineering &
Industrial Aerodynamics
THE JOURNAL OF THE
INTERNATIONAL ASSOCIATION FOR WIND ENGINEERING
EDITOR
Professor T. Stathopoulos, Concordia University, Montreal, Canada
Available online at www.sciencedirect.com
ScienceDirect
www.elsevier.com/locate/jweia

J. Wind Eng. Ind. Aerodyn. 98 (2010) 754–766

Contents lists available at ScienceDirect

Journal of Wind Engineering and Industrial Aerodynamics

journal homepage: www.elsevier.com/locate/jweia

Discrete vortex method simulations of the aerodynamic admittance in bridge aerodynamics

Johannes Tophøj Rasmussen [a], Mads Mølholm Hejlesen [a], Allan Larsen [b], Jens Honoré Walther [a,c,*]

[a] Department of Mechanical Engineering, Technical University of Denmark, Building 403, DK-2800 Kgs. Lyngby, Denmark
[b] COWI A/S, Parallelvej 2, DK-2800 Kgs. Lyngby, Denmark
[c] Computational Science and Engineering Laboratory, ETH Zürich, Universitätsstrasse 6, CH-8092 Zürich, Switzerland

ARTICLE INFO

Article history:
Received 22 April 2010
Received in revised form
23 June 2010
Accepted 29 June 2010

Keywords:
Discrete vortex method
Wind field simulation
Turbulence
Fluid structure interaction
Aerodynamic admittance
Flat plate

ABSTRACT

We present a novel method for the simulation of the aerodynamic admittance in bluff body aerodynamics. The method introduces a model for describing oncoming turbulence in two-dimensional discrete vortex method simulations by seeding the upstream flow with vortex particles. The turbulence is generated prior to the simulations and is based on analytic spectral densities of the atmospheric turbulence and a coherence function defining the spatial correlation of the flow. The method is validated by simulating the turbulent flow past a flat plate and past the Great Belt East bridge. The results are generally found in good agreement with the potential flow solution due to Liepmann.

1. Introduction

The discrete vortex method is widely used in academia and by the industry to model two-dimensional (2D) bluff body flows (Smith and Stansby, 1988; Koumoutsakos and Leonard, 1995; Cottet, 1990; Larsen, 1998a; Larsen and Walther, 1998; Taylor and Vezza, 2001; Zhou et al., 2002; Taylor and Vezza, 2009; Ge and Xiang, 2008). The discrete vortex method is a Lagrangian formulation of the Navier–Stokes equations governing the flow. The equations are solved by convecting and diffusing vortex particles carrying vorticity. A boundary element method may be used to enforce the no-slip condition at the solid boundaries and hence alleviates the time consuming mesh generation required in Eulerian methods. Moreover, the simulation of flow past multiple bodies undergoing arbitrary motion is straightforward. The 2D discrete vortex method implementation DVMFLOW (Walther, 1994) is an engineering tool, which has been used extensively by the consulting company COWI[1] to simulate the flow past bridge sections (Larsen and Walther, 1997; Larsen, 1998b; Vejrum et al., 2000; Larsen et al., 2008). The simulations provide detailed visualisation of the flow field and time history of the aerodynamic forces. Moreover, the aerodynamic derivatives and associated flutter limit are extracted from the simulations by imposing a prescribed heave and pitch motion of the bridge section (Larsen and Walther, 1998; Walther and Larsen, 1997). So far these studies have been limited to laminar flow simulations and only a few studies have considered the modeling of turbulence using 2D particle vortex methods cf. Alcântara Pereira et al. (2004) and Prendergast (2007). In the recent work of Prendergast and McRobie (2006) and Prendergast (2007), oncoming turbulence was modelled by seeding the free stream with vortex particles and simulations were performed to study buffeting in bridge aerodynamics. In the present work, we extend the model of Prendergast and McRobie to enable, for the first time, simulations of the aerodynamic admittance in bluff aerodynamics.The extension is performed within the DVMFLOW implementation.

2. Aerodynamic admittance

The influence of turbulence on the aerodynamic forces can be quantified by the aerodynamic admittance which is the focus of the present study. In the analysis of the aerodynamic admittance (Larose, 1997), the lift coefficient

$$C_L = \frac{L}{\frac{1}{2}\rho U^2 C}, \tag{1}$$

is assumed to be a linear function of the angle of attack (α), thus

$$C_L(\alpha) = C_{L_0} + C'_L \alpha, \tag{2}$$

* Corresponding author at: Department of Mechanical Engineering, Technical University of Denmark, Building 403, DK-2800 Kgs. Lyngby, Denmark.
Tel.: +45 45254327; fax: +45 4588 4325.
E-mail address: jhw@mek.dtu.dk (J.H. Walther).

[1] www.cowi.com

0167-6105/$ - see front matter © 2010 Elsevier Ltd. All rights reserved.
doi:10.1016/j.jweia.2010.06.011

where L denotes the lift force per unit length, C the chord length of the bridge section, ρ the density of the fluid, U the horizontal mean free stream velocity, and $C'_L \equiv \partial C_L/\partial\alpha$. For a fixed rigid structure, the instantaneous angle of attack (α) depends on U and the horizontal and vertical velocity fluctuations u and w, respectively, thus

$$\alpha \approx \frac{w}{U+u}. \tag{3}$$

By inserting the instantaneous velocity

$$U_i = \sqrt{w^2+(U+u)^2}, \tag{4}$$

into Eq. (1) and combining it with Eqs. (2) and (3) the lift force can be expressed as

$$L = \frac{\rho C}{2}(C_{L_0}U^2 + 2C_{L_0}Uu + C'_L wU), \tag{5}$$

where terms involving products of fluctuations have been neglected. Thus, the lift force due to the wind fluctuations becomes

$$L_f = \frac{\rho UC}{2}[2C_L u + C'_L w]. \tag{6}$$

Assuming that the force due to velocity fluctuations is a stationary random process, the equation can be transformed into the frequency domain (Larose, 1997):

$$S_{LL} = \left(\frac{\rho UC}{2}\right)^2 [4C_L^2 S_{uu}\chi_L^u + C'^2_L S_{ww}\chi_L^w], \tag{7}$$

where $\chi_L^u = \chi_L^u(\omega)$ and $\chi_L^w = \chi_L^w(\omega)$ denote the admittances due to the spectral density of the horizontal $S_{uu} = S_{uu}(\omega)$ and vertical $S_{ww} = S_{ww}(\omega)$ velocity fluctuations, and ω the angular frequency of the fluctuation. It is difficult to distinguish between the contribution from u and w, and instead the lumped aerodynamic admittance is defined:

$$\chi_L(\omega) = \frac{S_{LL}(\omega)}{(\frac{1}{2}\rho UC)^2[4C_L^2 S_{uu}(\omega) + C'^2_L S_{ww}(\omega)]}. \tag{8}$$

Often C_L is small compared to C'_L and the aerodynamic admittance can be reduced to a relation between the spectral density of the vertical velocity fluctuations S_{ww} and the lift force S_{LL}. That is, fluctuations in the lift force are mainly influenced by the vertical velocity fluctuations. For the pitching moment M the aerodynamic admittance can be derived analogously (Larose, 1997)

$$\chi_M(\omega) = \frac{S_{MM}(\omega)}{\left(\frac{1}{2}\rho UC^2\right)^2 [4C_M^2 S_{uu}(\omega) + C'^2_M S_{ww}(\omega)]}, \tag{9}$$

where

$$C_M = \frac{M}{\frac{1}{2}\rho U^2 C^2}, \tag{10}$$

and $C'_M = \partial C_M/\partial\alpha$.

In spite of the aerodynamic admittance generally being frequency dependent the constant transfer functions

$$S_{LL}(\omega) = \left(\frac{1}{2}\rho CUC'_L\right)^2 S_{ww}(\omega), \tag{11}$$

$$S_{MM}(\omega) = \left(\frac{1}{2}\rho C^2 UC'_M\right)^2 S_{ww}(\omega), \tag{12}$$

are often being used, assuming proportionality between the spectrum of the vertical fluctuations S_{ww} and the spectra S_{LL} and S_{MM} by C'_L and C'_M, respectively. This, in effect renders the aerodynamic admittance unity in the whole frequency range. The relation stems from potential theory with the lift force being the superposition of multiple lift force signals, each proportional to a sinusoidal vertical velocity fluctuation.

In the present work the flow past a flat plate and the flow past the Great Belt East bridge is simulated. By sampling time series of the velocity fluctuations, lift forces and pitching moments, the spectra S_{uu}, S_{ww}, S_{LL} and S_{MM} can be computed, and in turn the aerodynamic admittances χ_L and χ_M.

3. Vortex method

An incompressible flow with constant kinematic viscosity ν is governed by the 2D Navier–Stokes equations in vorticity form

$$\frac{D\omega_u}{Dt} = \frac{\partial\omega_u}{\partial t} + \boldsymbol{u}\cdot\boldsymbol{\nabla}\omega_u = \nu\Delta\omega_u. \tag{13}$$

The fluid velocity $\boldsymbol{u}$ is computed from the vorticity $\boldsymbol{\omega}_u = \omega_u \boldsymbol{e}_z$ and the stream function ψ:

$$\boldsymbol{\omega}_u = \boldsymbol{\nabla}\times\boldsymbol{u}, \tag{14}$$

$$\boldsymbol{u} = \boldsymbol{\nabla}\times(\psi\boldsymbol{e}_z), \tag{15}$$

Combining Eqs. (14) and (15) and assuming ψ to be divergence free leads to the Poisson equation

$$\Delta\psi = -\omega_u. \tag{16}$$

Eq. (16) forms the basis of hybrid vortex particle-mesh methods such as the Vortex-In-Cell algorithm (Birdsall and Fuss, 1969; Sbalzarini et al., 2006; Morgenthal and Walther, 2007; Chatelain et al., 2008). In the present study, the Poisson equation is solved using Green's function solution:

$$\psi(\boldsymbol{x}) = \Psi + \int G(\boldsymbol{x}-\boldsymbol{y})\omega_u(\boldsymbol{y})\,\boldsymbol{dy}, \tag{17}$$

$$\boldsymbol{u}(\boldsymbol{x}) = \boldsymbol{U} - \int \boldsymbol{K}(\boldsymbol{x}-\boldsymbol{y})\omega_u(\boldsymbol{y})\,\boldsymbol{dy}, \tag{18}$$

where Ψ is the far-field stream function, and G and $\boldsymbol{K}$ the corresponding 2D Green's functions:

$$G = -\frac{1}{2\pi}\log|x|, \tag{19}$$

$$\boldsymbol{K} = \frac{1}{2\pi}\frac{\boldsymbol{x}}{|\boldsymbol{x}|^2}\times . \tag{20}$$

The vorticity field is approximated by discrete vortex particles carrying circulation:

$$\Gamma = \int_{\mathcal{A}} \omega_u\,dA = \int_{\mathcal{S}} \boldsymbol{u}\cdot\boldsymbol{ds}, \tag{21}$$

where $\mathcal{A}$ is the area of the particle bounded by $\mathcal{S}$. The vorticity field is discretized by a superposition of N discrete vortex particles:

$$\omega_u^\varepsilon(\boldsymbol{x}) = \sum_i^N \zeta_\varepsilon(\boldsymbol{x}_i-\boldsymbol{x})\Gamma_i, \tag{22}$$

where $\zeta_\varepsilon(\boldsymbol{x})$ is a smooth approximate to the Dirac delta function: $\zeta_\varepsilon(\boldsymbol{x}) = (1/\varepsilon^2)\zeta(|\boldsymbol{x}|/\varepsilon)$, and ε is the smoothing radius. The present study uses the second order Gaussian kernel: $\zeta(r) = (1/2\pi)e^{-r^2/2}$ cf. e.g. Winckelmans and Leonard (1993).

The discrete kinematic relation governing the flow is obtained from Eqs. (18) and (22):

$$\boldsymbol{u}(\boldsymbol{x}) = \boldsymbol{U} - \sum_i^N \boldsymbol{K}_\varepsilon(\boldsymbol{x}-\boldsymbol{x}_i)\times\Gamma_i\boldsymbol{e}_z, \tag{23}$$

where $\boldsymbol{K}_\varepsilon = -(q_\varepsilon(\boldsymbol{x})/|\boldsymbol{x}|^2)\boldsymbol{x}$ is the smooth velocity kernel, and $q_\varepsilon(\boldsymbol{x}) = q(|\boldsymbol{x}|/\varepsilon)$, and $q(r) = (1/2\pi)(1-e^{-r^2/2})$.

The motion and strength of the discrete particles is solved using viscous splitting (Chorin, 1973). Hence, the particles are first convected:

$$\frac{d\boldsymbol{x}_p}{dt} = \boldsymbol{u}(\boldsymbol{x}_p), \tag{24}$$

$$\frac{d\boldsymbol{\omega}_u}{dt} = 0, \tag{25}$$

and subsequently diffused:

$$\frac{d\boldsymbol{x}_p}{dt} = 0, \tag{26}$$

$$\frac{d\boldsymbol{\omega}_u}{dt} = \nu\Delta\boldsymbol{\omega}_u. \tag{27}$$

In the present DVMFLOW implementation, the convection step is solved using first or second order explicit time integration schemes, and diffusion is modeled using the method of random walks (Chorin, 1973). Hence, after the convection step (Eq. (24)), the position of the vortex particles is perturbed with a random displacement, drawn from a normal distribution with zero mean and variance $2\nu\Delta t$. Δt denotes the simulation time step.

The solid boundaries are discretized using a boundary element technique (Wu, 1976; Wu and Gulcat, 1981). The no-penetration condition is enforced by determining the strength of the vortex sheets (γ) on the panels, which forms a linear system of equations. A unique solution is obtained by imposing Kelvin's circulation theorem (Walther and Larsen, 1997):

$$\sum \Gamma = 0. \tag{28}$$

The introduction of upstream vortex particles with a total non-zero circulation Γ_T requires a modification of Eq. (28) such that $\sum \Gamma = \sum \Gamma_T$.

The computational efficiency of the discrete vortex method is closely related to the solution of the N-body problem implied by Eqs. (23) and (24) which nominally scales as $O(N^2)$. The present implementation uses the fast multipole method (Greengard and Rokhlin, 1987; Carrier et al., 1988) to achieve an optimal $O(N)$ scaling.

The forces and moments are calculated from the pressure distribution which in turn is calculated from the distribution of the vortex sheet along the boundary s:

$$\frac{1}{\rho}\frac{\partial p}{\partial s} = -\frac{\partial \gamma}{\partial t}. \tag{29}$$

The derivatives C'_L and C'_M are found by finite differences of C_L and C_M measured at different angles of attack assuming either a laminar or turbulent oncoming flow. Laminar flow simulations are used similar to the practice of wind tunnel testing.

4. Synthesizing turbulence

To introduce turbulence into the oncoming flow of a simulation a time series of vortex particles is generated prior to the simulation (Prendergast and McRobie, 2006). These particles are inserted into the flow during the simulation at a fixed insert rate. The vortex particles are convected downstream forming a band of particles which induce turbulent velocity fluctuations. Initially turbulent velocity series are generated on the nodes of a regular vertical grid using the Shinozuka–Deodatis method (Shinozuka and Jan, 1972; Deodatis, 1996), and in accordance with the spectral densities of the atmospheric velocity fluctuations. The grid consists of N_p vertically aligned quadratic cells, see Fig. 1. In each point two velocity time series are generated: one in the streamwise (horizontal) direction and another in the crosswise (vertical) direction, u and w, respectively. Presently these velocity

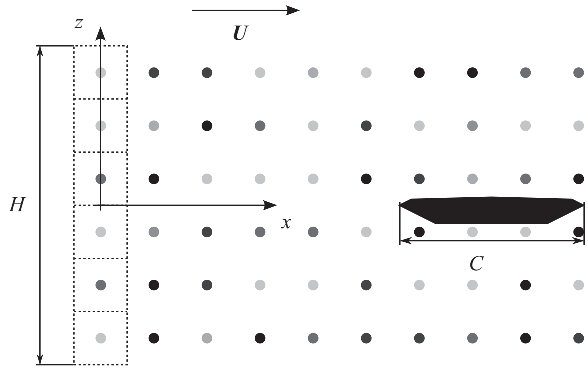

Fig. 1. From the grid at the left vortex particles are released and convected downstream by the flow induced by the vortex particles of the flow and the free stream velocity U. Coordinates (x,z) are given relative to the center of the grid of height H, and (u,w) are the respective velocity components. Solid objects with a chord length C inserted in the flow are placed on the x-axis.

time series are based on the modified von Kármán spectra of the Engineering Sciences Data Unit (1993) (ESDU), see Appendix A. Atmospheric turbulence is anisotropic, thus two spectra are needed: one for the horizontal and another for the vertical fluctuations. The magnitude and distribution of the spectra depend on various physical parameters such as the surface roughness length scale (z_0), the height above ground level (h), and the free stream velocity (U). However, the available parameters can only be varied within a certain range and with limited influence on the turbulence intensity

$$I_u = \frac{\sigma_u}{U},$$

$$I_w = \frac{\sigma_w}{U}. \tag{30}$$

Hence, varying the physical parameters mostly influences the magnitude of the atmospheric velocity spectral density while the distribution is largely unaffected cf. Clementson (1950) and Fung (1955). Therefore to obtain a specific turbulence intensity $\tilde{I}_w = \tilde{\sigma}_w/U$ the analytic spectral density $S_{ww}(\omega)$ is scaled

$$\tilde{S}_{ww}(\omega) = \left(\frac{\sigma_w}{\tilde{\sigma}_w}\right)^2 S_{ww}(\omega), \tag{31}$$

to match the target intensity:

$$\int \tilde{S}_{ww}(\omega)\, d\omega = \tilde{\sigma}_w^2. \tag{32}$$

The spectral densities are discretized in N_f discrete frequencies

$$\omega_k = k\Delta\omega, \quad k = 0,1,\ldots,N_f-1, \tag{33}$$

with a uniform spacing

$$\Delta\omega = \frac{\omega_{max}}{N_f}. \tag{34}$$

The upper cut-off frequency ω_{max} is chosen such that the energy of the discarded frequency range is negligible. Furthermore the Nyquist criterion

$$\omega_{max} \le \frac{\pi}{\Delta t_{\text{gen}}}, \tag{35}$$

is fulfilled to avoid aliasing. Δt_{gen} is the time step at which velocities are generated on the grid, and $1/\Delta t_{\text{gen}}$ is the corresponding insert rate.

The velocity series in the points m and n on the grid are spatially correlated through the coherence function (Davenport, 1968; Rossi et al., 2004)

$$\mathrm{Coh}_{u_m u_n}(\omega) = e^{-\hat{f}}, \tag{36}$$

with the decay function

$$\hat{f} = \frac{\omega}{2\pi} \frac{\sqrt{C_{ux}^2 (x_m - x_n)^2 + C_{uz}^2 (z_m - z_n)^2}}{0.5(U(z_m) + U(z_n))}, \tag{37}$$

where $C_{ux} = 3$ and $C_{uz} = 10$ are decay coefficients (Simiu and Scanlan, 1996). The spatial correlation for the vertical velocities is analogous to Eqs. (36) and (37), and the decay coefficients are assumed $C_{wx} = C_{ux}$, $C_{wz} = C_{uz}$ (Prendergast, 2007). Hereby the influence of a velocity series in m to a series in n becomes

$$S_{u_m u_n}(\omega) = \sqrt{S_{u_m u_m}(\omega) S_{u_n u_n}(\omega)} \mathrm{Coh}_{u_m u_n}(\omega) e^{i\theta_{u_m u_n}(\omega)}. \tag{38}$$

The angular phase shift

$$\theta_{u_m u_n}(\omega) = \omega \frac{x_n - x_m}{U}, \tag{39}$$

is defined in correspondence with Taylor's Hypothesis, i.e. the phase shift is equal to the duration for the flow to move between the points m and n times the frequency. It is seen that $S_{u_m u_n}$ is given directly from S_{uu} for m=n. It is assumed that there is only spatial correlation between velocity components in the same direction (Prendergast, 2007), i.e. that there is no correlation between the u and w velocities. The contribution of all velocities to each other is contained in the cross spectral matrix:

$$\boldsymbol{S}(\omega) = \begin{bmatrix} [S_{u_m u_n} \ m,n \le N_p] & \boldsymbol{0} \\ \boldsymbol{0} & [S_{w_m w_n} \ m,n \le N_p] \end{bmatrix}, \tag{40}$$

We let m be the index of a velocity process in a point and by velocity process understand a velocity series either horizontal or vertical. It follows that there will be twice the number of velocity processes as the number of points in the grid N_p. Then

$$f_m(t) = \sqrt{2\Delta\omega} \sum_{n=1}^{2N_g} \sum_{k=1}^{N_f - 1} |H_{mn}(\omega_k)| \cos\beta(t),$$

$$\beta(t) = \omega_k t + \theta_{mn}(\omega_k) + \phi_{nk}, \tag{41}$$

is the mth velocity process (Shinozuka and Jan, 1972) found by summing a series of N_f cosine waves from each of the $2N_p$ velocity processes, including m. In effect the summation over m is only to N_p with no correlation between vertical and horizontal velocities in the cross spectral matrix $\boldsymbol{S}(\omega_k)$ cf. Eq. (40). The amplitudes of the cosine waves are determined from the Cholesky decomposition $\boldsymbol{H}(\omega_k)$ of $\boldsymbol{S}(\omega_k)$. Furthermore

$$\theta_{mn}(\omega_k) = \arctan\left(\frac{\mathrm{Im}[H_{mn}(\omega_k)]}{\mathrm{Re}[H_{mn}(\omega_k)]}\right), \tag{42}$$

is the complex argument of $H_{mn}(\omega_k)$ and ϕ_{nk} is a random phase in the interval $[0; 2\pi]$.

The efficiency of the process is significantly improved by using fast Fourier transforms (FFTs) to carry out the summation (Deodatis, 1996). The velocity series becomes

$$f_m(t_r) = \sqrt{2\Delta\omega} \sum_{n=1}^{N_p} \mathrm{Re}[C_{mnr}], \tag{43}$$

where

$$C_{mnr} = \sum_{k=0}^{2N_f - 1} c_{mnk} e^{i(2\pi/2N_f)kr}, \tag{44}$$

is the Fourier transform of

$$c_{mnk} = |H_{mn}(\omega_k)| e^{i(\theta_{mn}(\omega_k) + \phi_{nk})}. \tag{45}$$

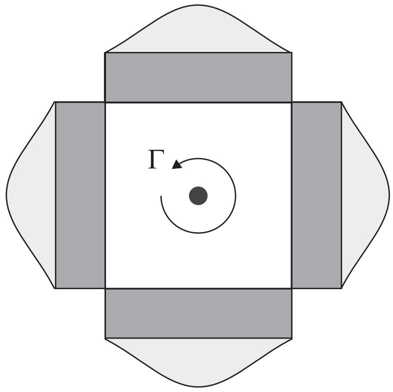

Fig. 2. The circulation from a point vortex integrated with the corner point approximation on a cell with side length Δx is marked by the dark gray area. The actual non-linear distribution $d\Gamma/ds = \Gamma_{\mathrm{vortex}}/\pi\Delta x(s^2+1)$, $s \in [-1;1]$ is the unification of the dark and the light gray areas.

Using the maximum discrete time step that fulfills the Nyquist criterion Eq. (35), the discrete time becomes

$$t_r = r\Delta t_{\mathrm{gen}}, \quad r \in [0; 2N_f - 1]. \tag{46}$$

For each of the quadratic cells of the grid the circulation is integrated from the grid node velocities using the trapezoidal rule (Prendergast, 2007). The circulation is corrected in magnitude by a factor K such that

$$\Gamma = K\Gamma_{\mathrm{trapezoidal}}. \tag{47}$$

This accounts for the mismatch between the linear assumption of the integration and the actual circular velocity contours of a point vortex. The actual distribution of circulation from a singular point vortex of strength Γ_{vortex} on a cell with side length Δx is not linear but given by

$$\frac{d\Gamma}{ds} = \frac{\Gamma_{\mathrm{vortex}}}{\pi\Delta x(s^2+1)}, \quad s \in [-1; 1], \tag{48}$$

see Fig. 2. By integrating Eq. (48) around the cell boundary it is seen that $\Gamma = \Gamma_{\mathrm{vortex}}$ if $K = \pi/2$. For each cell a particle is associated with the corresponding circulation and inserted during the flow simulation at every $\Delta_p = \Delta t_{\mathrm{gen}}/\Delta t$ time step. The side length of the quadratic cells $\Delta x = \Delta_p \Delta t U$ corresponds to the distance the particles are convected by the free stream velocity between subsequent particle releases. As the particles are being convected downstream they form a band of particles with a total non-zero circulation $\sum \Gamma_T$. The final condition for the panel strength of the boundary elements Eq. (28) is modified such that $\sum \Gamma = \sum \Gamma_T$. Imposing total zero circulation would otherwise affect the panel strengths and render force calculation by surface pressure distribution impossible. Alternatively the particle strengths can be modified by subtracting the mean particle turbulence circulation from the particles being released such that no net circulation is added. However, this disrupts the streamwise correlation between the particles and leads to strongly reduced energies in the low frequency region of spectral density of the resulting simulation velocities.

5. Validation and results

We perform simulations of the turbulent flow past a flat plate and past the Great Belt East bridge to test and validate the current implementation. The admittance for the flow past the flat plate serves as a reference case and allow systematic variation of the key numerical parameters. The reference parameters related to the discretization of the spectral density of atmospheric turbulence is the upper angular frequency $\omega_{max} = 36.7\,\text{rad/s}$ and the number of discrete frequencies N_f=4096. When integrating the grid velocities to particle strength a correction factor $K = \pi/2$ is used. The variation of the spectra with respect to the point of sampling is examined, and the dependency of the number of particles N_p per release as well as the particle insert interval Δ_p is investigated. Reference values for these parameters are N_p=120 and $\Delta_p = 4$.

The atmospheric turbulence is reconstructed from the ESDU spectra, defined in Appendix A using the reference parameters. The reference spectra are subsequently scaled to meet a specified vertical turbulence intensity of I_w=5%.

When introducing a solid structure into the flow we also introduce an additional length scale, i.e. the chord length (C), and hence the Reynolds number $\text{Re} = UC/\nu$. We study the influence of Re and turbulence intensity I_w on the aerodynamic admittance. As reference the flow is simulated at Re=10,000 to ensure a relatively thin boundary layer and to allow comparison with the potential flow solution. For the boundary layer to remain stable (Walther and Larsen, 1997) and to ensure sufficient spatial resolution the simulations are not carried out at higher Reynolds numbers. The relevant Reynolds number for full scale bridges is $\mathcal{O}(10^8)$ and for the wind tunnel tests typically $\mathcal{O}(10^5)$. However, to allow comparison with the results obtained for the flat plate we maintain Re=10,000 for the bridge simulations.

The velocity time series and particle strengths are generated in SI-units and non-dimensionalized before being used as input for the DVMFLOW simulations. As characteristic length a typical value for the bridge chord length C=30 m is used, for both bridge section and the flat plate benchmark. The characteristic free stream velocity is U=35 m/s which is a typical design wind speed in bridge engineering. The recorded velocities, forces and pitching moments are re-dimensionalized and analysed. As the aim of this text is to investigate flow properties of solid objects all positions have been given in units of C. For comparison purposes this is also the case when investigating the flow when no solid body is present.

Spectral densities are statistical properties of a sample or a signal and often contain a significant amount of noise. To reduce noise the signals have been subsampled with 50% overlap and the resulting spectra averaged. This significantly improves the consistency of the spectra but at the cost of reduced low-frequency information. Further noise reduction can be achieved by applying window functions at the cost of uncertainty in the magnitude of the spectra (Harris, 1978). Window functions preserve the shape of the spectrum and reduce noise, thus admittances have been calculated from spectra based on windowed samples, as any change of the magnitude cancels out. Before sampling any velocity and force the simulation is carried out until both the sampling points and the structures are well immersed in the turbulent flow. Most signals in the present work consist of 38,000 samples which are divided into 2–10 subsamples. Though some uncertainty remains, this reduces noise significantly at the cost of the frequency range. To be able to compare similar spectra in the same figure, approximations by N-point Bézier curves have been used to remove noise when necessary. N-point Bézier curves use all N samples for the approximation. Certain cases have been run extensively with a total of 380,000 samples. This allows increased subsampling and in turn accurate spectra in a wide frequency range. The typical range of interest for structural analysis of long span bridges is 0.05–1.0 Hz. For pedestrian bridges the range of interest is typically in the range of 0.5–5.0 Hz. In angular frequency these intervals are 0.31–6.3 and 3.14–31.4 rad/s, respectively. In the following the terms: low-, mid- and high-range frequencies refer approximately to the frequency intervals separated by $\omega = 0.8$ and 10 rad/s.

5.1. Power spectral density of the velocity

When generating the upstream particles many parameters influence the simulated turbulent velocities. The optimal value of the numerical parameters is not necessarily obvious, nor can they be chosen freely due to computational constraints. These parameters are investigated in this section.

5.1.1. Sensitivity to upper cutoff and spectral resolution

The upper cutoff of the frequency (ω_{max}) and the finite number of discrete frequencies (N_f) at which the velocity spectrum is defined will affect the resulting velocity signal. Both the velocity signal on the grid and in turn the vortex induced velocities in the simulation are affected. We study these parameters in the following and compare the result with theoretical values.

The upper cutoff (ω_{max}) is chosen above the frequency range of interest such that the turbulent energies σ_u^2 and σ_w^2 are conserved to the extent possible. Fig. 3a shows the discarded energy

$$\eta(\omega_{max}) = \left(1 - \frac{1}{\sigma^2}\int_0^{\omega_{max}} S\,d\omega\right) \times 100\%, \tag{49}$$

as a function of ω_{max}. Thus, the reference cutoff $\omega_{max} = 36.7\,\text{rad/s}$ entails a loss of horizontal turbulent energy of $\eta_u = 1.7\%$ and $\eta_w = 6.7\%$ vertical velocity energy. For the vertical velocity energy loss to be reduced to 1% the upper cutoff must be approximately 20 times higher. Thus for a constant $\Delta\omega$ the complete energy of the spectrum cannot be expected to be preserved as the memory requirements scale as $\mathcal{O}(N_f N_p^2)$.

To conserve the energy of the spectra for $\omega \leq \omega_{max}$ a sufficient number of discrete frequencies (N_f) is required. Fig. 3b shows the turbulence intensities I_u and I_w of the grid velocity series as a function of N_f. The turbulence intensities have been normalized by $I_u\sqrt{1-\eta_u}$, the expected values corrected by the effect of the upper

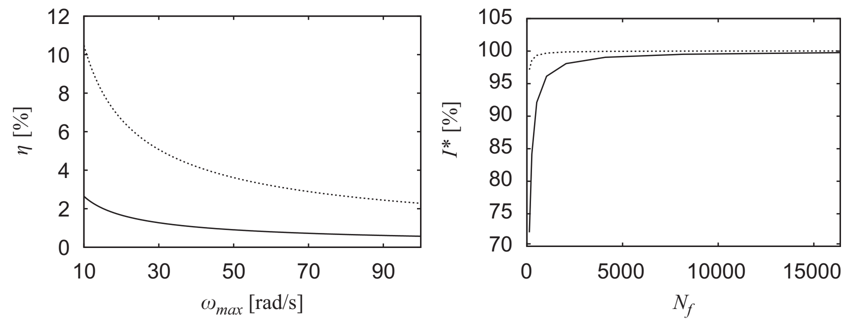

Fig. 3. (a) Deficiency of energy $\eta = (1 - \int_0^{\omega_{max}} S\,d\omega/\sigma^2) \times 100\%$ as a function of upper cutoff ω_{max} for the spectral density of the horizontal (——) and vertical (- - - - - -) velocities. (b) Normalized turbulence intensity $I^* = I_{RMS}/I_{target} \times 100\%$ for the horizontal (——) and vertical (- - - - - -) velocity time series on the grid as a function of the number of discrete frequencies N_f. The energy loss due to ω_{max} has been accounted for in I_{target}.

cutoff. The vertical turbulence intensity I_w converges faster than I_u and for N_f=4096 they are 99.96% and 99.04% of the expected values, respectively. The energy loss from the finite frequency range is more significant than that caused by the resolution of the spectrum. In addition we find that the grid velocities are in good agreement with the prescribed spectra, both in terms of the turbulent energy σ_u^2 and σ_w^2 and also the spectral distribution: S_{uu} and S_{ww} (not shown).

5.1.2. Effects of frequency discretization and circulation integration

While the energy of the time series of the grid velocity is a first indicator of the validity of the synthesis, the spectral density of the velocity time series sampled during the simulation shows more detail of the method, cf. Fig. 4. In the following we study the effect of the discrete frequencies (N_f) on the velocity spectra sampled during the simulation.

Both the horizontal (S_{uu}) and vertical (S_{ww}) spectra show a significant dependency on the number of discrete frequencies N_f, see Figs. 4a and b, respectively. For both the horizontal and vertical spectra, the high frequency range has converged at just 128 discrete frequencies. The higher the spectral resolution the further the spectra converge into the low frequency range and for $N_f \geq 2048$ the spectra have converged for all but the very lowest frequencies. The atmospheric turbulence spectra have been discretized with the lowest non-zero discrete frequency $\Delta\omega$. $\Delta\omega$ is indicated for each spectral resolution by a vertical line patterned similarly to the corresponding spectrum, and below $\Delta\omega$ the sampled spectra contain little energy. For the coarse discretization (N_f=128) the discrete frequencies are clearly visible, indicating that exactly the frequencies of interest are preserved by the conversion from grid velocities to particle induced velocities. We choose N_f=4096 as a compromise between accuracy in the low frequency range and the required memory and computational resources.

The spectral densities of the time series of the grid velocity show perfect match to the target spectra (not shown), whereas the spectral density of the simulation deviate from the target. Hence the deviations are a result of the method of converting grid velocity to particle strengths and the finite release rate of the upstream particles. The strongly deviating low frequency range energy of S_{ww} is observed only for the frequencies at which the atmospheric turbulence spectrum has been discretized, Fig. 4. This indicates that the deviation is primarily an effect of converting grid velocities to particle strengths and not an effect of the actual release of particles during the simulation. The latter is investigated in Section 5.1.6. It is worth noting how well the values of the discrete frequencies are preserved in the process of converting grid velocities to particle strengths. S_{ww} is above target for the whole frequency range, see Fig. 4b, as is also the case for S_{uu} except for the low frequency region in which S_{uu} is lower than the target, see Fig. 4a.

5.1.3. Influence of circulation correction

The correction factor, $K=\pi/2$ cf. Eq. (47), is based on the simple comparison of the integral over the grid velocity induced by a single vortex particle to the strength of the vortex particle. The spectra of the simulated velocities have been observed to be greater than their target, and we therefore investigate the effect of varying K. The variance of the sampled horizontal velocity signal σ_u^2 is below target and above target for the vertical velocity signal σ_w^2. This corresponds to the deviations in the low frequency range of S_{uu} and S_{ww}, respectively, see Fig. 4. Outside the low frequency range the spectra are generally above the target by a constant factor ≈ 1.25. However, the distribution is correct indicating that the conversion from grid velocities to particle strengths is valid in this region and that the offset is caused by the circulation correction K. By varying K the spectra can be offset uniformly by a factor as seen in Fig. 5. Thus, K can be adjusted to achieve better agreement between the spectral density of the sampled velocity and the target. As expected the variance scales proportionally with K^2, hence (σ_u,σ_w) equals (4.87,4.17), (6.13, 5.36), and (11.0, 8.23) for $K=0.70\pi/2$, $0.85\pi/2$, and $1.00\pi/2$, respectively.

5.1.4. Spatial dependency

The velocity field induced from a vortex particle is purely tangential relative to the position of particle cf. Eq. (23). Hence, the horizontal velocity component at a point is mainly induced by particles vertically aligned with the point and vice versa. Ideally a sample point should be surrounded with a larger number of vortex particles to ensure convergence of the turbulent energies of both the horizontal and vertical components. However, a finite distance to the edge of the particle band is sufficient as other effects, such as viscous diffusion, become more dominant than the contribution from far-field particles. We study this effect by considering the variation of the spectral energy as a function of the position relative to the release grid. We do this by sampling at different positions on the centerline of the particle band, downstream of the release grid, $x=1C,2C,4C,\ldots,128C$. As the horizontal velocities mainly depend on particles vertically aligned with the sampling point, the energy σ_u^2 increases and converges quickly with respect to the downstream position x (not shown). Due to the strong dependency of the vertical velocity to the particles downstream and particularly upstream, σ_w^2 increases with x and converges approximately 16 times farther downstream than σ_u^2, at $x=32C$ (not shown).

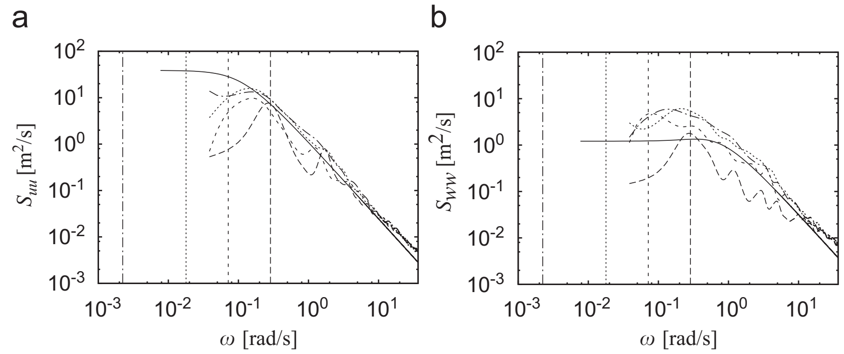

Fig. 4. The spectral density (a) S_{uu} and (b) S_{ww} of the velocity from the simulations, using turbulence series based on analytic spectra with varying number of discrete frequencies N_f: 128 (— — — — —), 512 (– – – – – –), 2048 (- - - - - -), and 16,384 (— - — - — -). The target spectrum (———) is shown as reference. The highest frequency in the range is ω_{max}. The spectra are averages from 10 subsamples and have been smoothened by N-point Béziers.

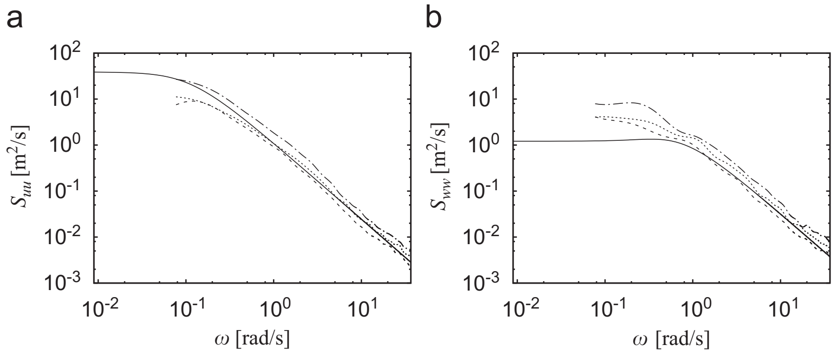

Fig. 5. Spectral density of the (a) horizontal velocity S_{uu} and (b) vertical velocity S_{ww} for circulation integral correction (Eq. (47)) of $K=0.70\pi/2$ (— — — — — —), $K=0.85\pi/2$ (------), $K=1.00\pi/2$ (—-—-—-—-—) and target (———). The spectra have been plotted in the range of the discrete frequencies used for turbulence generation.

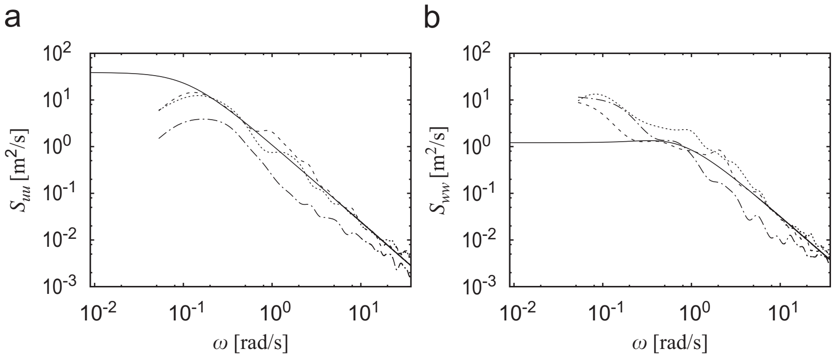

Fig. 6. Spectral densities (a) S_{uu} and (b) S_{ww} of the velocity field sampled on the particle band centerline: 2C (— — — — — —), 32C (---------), 128C (—-—-—-—-) downstream of the release grid. The height of the grid is 12C. The signal has been subsampled twice and the spectra smoothened by N-point Béziers. The spectra have been plotted in the range of the discrete frequencies used for turbulence generation.

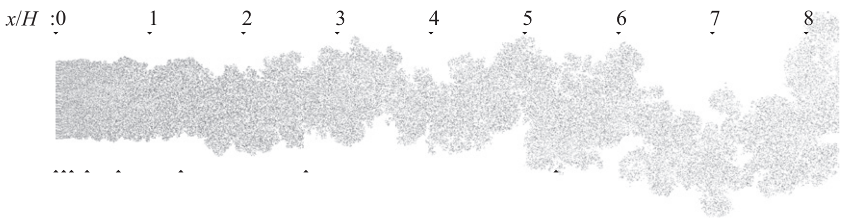

Fig. 7. Flow visualization in the range from $x=0C$ to 100C. The downstream distance is marked in units of particle band heights H (above). Below the particle band the x-coordinates of the sampling points of Section 5.1.4 have been marked. The height of the release grid is $H=12C$.

The influence of x on σ_w^2 is predominant and the increased energy is located mainly in the low frequency range of S_{ww} cf. Fig. 6b. Immediately downstream of the release grid, and until $x\approx 8C$ (not shown), the energy of the high frequency ranges grows from approximately 70% below to 70% above target. At this point the spectrum has converged for all but $\omega < 0.25$, in which frequency range the energy grows continuously as the flow is convected. For sampling points in the range 16C–45C, S_{ww} remains unchanged and the sampling point can be considered sufficiently immersed in the turbulent flow, and sufficiently far from the rotation-free flow upstream of the release grid. After 45C the spectral energy gradually decreases. Initially in the mid range frequencies but eventually extending to the entire spectrum. Fig. 7 indicates that this is due to mixing of rotation free flow towards the centerline of the particle band.

The standard deviation of the horizontal fluctuations σ_u^2 is below target which is primarily due to the energy of the low frequency range of S_{uu}. It is conjectured that a higher particle band would cause a similar deviation of S_{uu} to the target as that of S_{ww}, i.e. stronger low frequency energy. Due to memory constraints the particle band height of the reference flow is limited to 12C, i.e. to 15% of the distance required for σ_w^2 to converge. S_{uu} converges at $x=2C$, considerably faster than S_{ww}. As the flow is convected downstream the horizontal turbulent energy diminishes as shown in Fig. 6a. From $x=8C$ the energy of the mid-range frequencies decreases slightly and further downstream, at $x=64C$ the entire frequency range of S_{uu} decays almost uniformly.

The aerodynamic admittance has a stronger dependence on S_{ww} than on S_{uu} and any solid objects to be investigated in the present work is placed with the leading edge at $x=20C$. Hereby the object is immersed in a region of the flow with constant spectral properties and a representative velocity signal can be sampled upstream of the object. When sampling 4C upstream of the leading edge neither the plate nor the Great Belt East bridge section has any significant influence on the spectral densities of the sampled velocities.

Sampling will be performed on the centerline of the particle band. Sampling off of the centerline of the 12C high particle band at $x=16C$ shows only insignificant influence when e.g. sampling 4C off the centerline, i.e. 2C from the edge of the particle band (not shown). The deviation is only for the very lowest frequency range and mainly in the horizontal velocity spectrum S_{uu}. This suggests that the finite grid height $H=12C$ leaves a broad vertical margin in which the flow is spectrally uniform. This does not mean that a particle band height of $2\times 2C$ is sufficient as will be seen in Section 5.1.5.

5.1.5. Dependency of grid height

The band of particles must be of a certain height for a structure to be exposed to a flow with the properties of atmospheric turbulence. The required height of the particle band is investigated by keeping the insert interval Δ_p fixed thereby not changing the particle density. The height of the release grid is varied from 3C to 12C corresponding to 30 to 120 vortex particles per release.

The energy of the horizontal turbulent fluctuations increases due to the influence of the higher band of upstream particles. As Fig. 8a indicates increasing the grid height causes a consistent increase of turbulent energy in the low frequency range of the energy spectrum. This indicates that the height of the particle band limits large low frequency structures.

There is not a similar consistent relation between the magnitude of the vertical turbulent energy and the grid height, as shown in Fig. 8b. The vertical turbulent energy σ_w^2 grows downstream of the release grid until it converges. For all grid heights σ_w^2 starts to decay at approximately 3.5 times the grid height for the present settings. This corresponds well to the mixing of rotation free flow towards the centerline of the particle band as shown in Fig. 7.

5.1.6. Dependency of inter-particle spacing

The band of particles must be sufficiently densely filled and the distance between particles at the release grid is determined by the width of the release grid cells. As described in Section 4 the width of the cells is proportional to the free-stream velocity and the interval with which particles are inserted into the stream Δ_p. Thus Δ_p controls the density of particles and by decreasing the particle insert interval Δ_p, particles are being inserted at a higher rate. Since the cells of the release grid are quadratic, the particles will be more closely spaced in both the streamwise and vertical directions. The number of particles per release strongly influences the computational requirements, thereby limiting the height of the particle band. Thus to be able to set $\Delta_p=1$ a particle band of height 3C is used with the entailing energy deficiencies described in Section 5.1.5.

By varying the rate with which particles are released into the flow it has been observed that an increased energy in the high frequency range follows an increase of the particle insert interval Δ_p. When sampling velocities directly at the release grid the frequency of the particle release

$$\omega_{release}=\frac{2\pi}{\Delta t\Delta_p}, \tag{50}$$

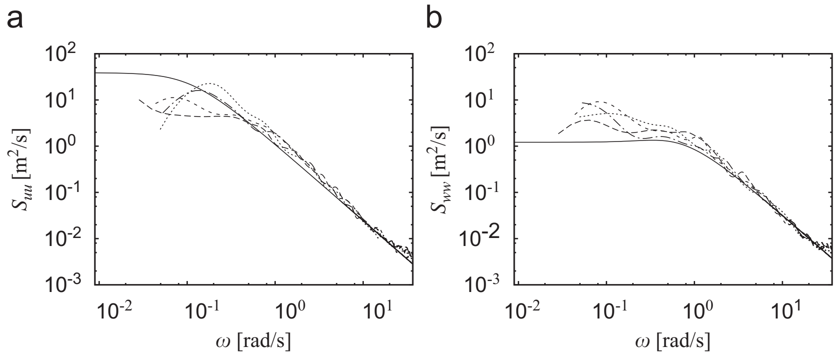

Fig. 8. Spectral density for the (a) horizontal S_{uu} and (b) vertical S_{ww} velocities, for varying release grid height 3C and 30 points (——————), 6C and 60 points (– – – – – –), 9C and 90 points (---------), 12C and 120 points (—-—-—-). The signal is sampled 10C downstream of the release grid and has been subsampled five times and the spectra averaged. The spectra have been plotted in the range of the discrete frequencies used for turbulence generation.

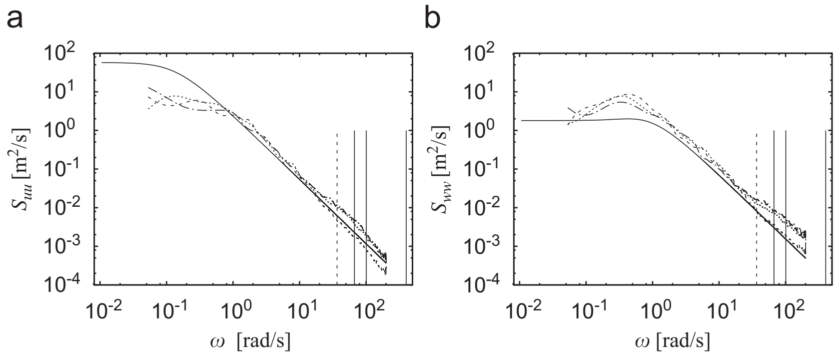

Fig. 9. Spectral density of the (a) horizontal velocities S_{uu} and (b) vertical velocities S_{ww} sampled 10C downstream of grid. The insert interval is varied between 1 (— — — — — —), 4 (---------), and 6 (—-—-—-). The vertical long-dashed line marks ω_{max}, the solid lines mark $\omega_{release}$ corresponding to $\Delta_p=6$, $\Delta_p=4$, $\Delta_p=1$ from left to right. Due to memory constraints a fixed release grid height of $\approx 3C$ has been used to allow insertion every time step ($\Delta_p=1$). The spectra are averages of five subsamples and have been smoothened by an N-point Bézier.

is visible as a well-defined spike. Further downstream the energy of the spike spreads to the surrounding frequency range obscuring the spectral position of $\omega_{release}$. At $x=10C$ the positions of the energy spikes corresponding to $\Delta_p=4$ and 6 can no longer be distinguished, but the energy has spread to frequencies lower than the upper cutoff frequency ω_{max} as shown in Fig. 9. $\omega_{release}$ corresponding to $\Delta_p=1$ is outside the visible range. Setting $\Delta_p=1$ removes the artificial high frequency energy for $\omega<\omega_{max}$ and though this gives better agreement with the respective targets, it restricts the height of the release grid due to memory constraints. Furthermore the added energy is far above the frequency range of interest when looking at cable bridges or pedestrian bridges. In spite of the deviation of the high frequency range of the spectra the aerodynamic admittance shows good agreement with target cf. Section 5.2. In the present work large cable bridges are of interest and $\Delta_p=4$ is chosen as this gives little deviation of the spectra in the high frequency range and ensures a sufficient height of the particle band.

5.2. Aerodynamic admittance of a flat plate

5.2.1. Comparison with analytic solution

The flow past an infinitely thin plate is well studied in potential flow theory (Theodorsen, 1935; von Kármán and Sears, 1938), and by approximating the potential flow conditions the plate serves as a suitable benchmark. By assuming the vertical fluctuations to be small compared to the mean speed of the flow the admittance has been approximated by Liepmann (1952)

$$\chi_L=\frac{1}{1+(\pi C/U)\omega}. \tag{51}$$

In the present study, the potential flow past an infinitely thin plate subjected to an oncoming turbulent flow is approximated by the viscous flow past a flat plate of finite length and thickness. The viscous diffusion is modeled using random walks and hence the turbulent velocity fluctuation should be above a certain level for the turbulent velocity fluctuations to dominate the fluctuations of the viscosity modeling at the solid surface. Due to the finite thickness of the plate, the viscous flow and the turbulent fluctuations causing instantaneous angles of attack of up to 12°, separation occurs around the plate, see Fig. 10. In the present work a plate thickness $D=1/200C$ has been used. Since the requirements for the potential flow solution are not fully met, some deviation is anticipated. The measured slopes of the lift (C'_L) and pitching moment (C'_M) are $C'_L=5.5$ and $C'_M=-1.18$, respectively. The experimental values (Larose and Livesey, 1997) obtained for a plate with a chord-to-thickness ratio of $C/D=16$ are $C'_L=5.8$ and $C'_M=-1.43$, and thus a deviation less than 5% and 17%, respectively.

Fig. 11 shows the spectral densities for the horizontal (S_{uu}) and vertical (S_{ww}) velocities, the lift force S_{LL} and the pitching moment S_{MM}, as well as the corresponding aerodynamic admittance of the lift force χ_L and pitching moment χ_M. The velocity spectra agree with the results obtained in Section 5.1. The lift force spectrum S_{LL} and pitching moment spectrum S_{MM} have been plotted with the predicted spectra from the frequency independent relation, Eqs. (11) and (12) as reference. The reference spectra are based on the assumption of a frequency independent admittance and from Figs. 11c and d it is seen that the spectra cross the reference spectra. Except from the area of intersection of the spectra, neither their magnitudes nor their slopes match. In spite of the aerodynamic admittance generally being frequency dependent the frequency independent assumption is widely used as an initial approximation. In the low frequency range an increase of the spectral energy, similar to that of S_{ww}, can be seen in both S_{LL} and S_{MM}. This indicates that the forces on the plate are reactions to these added low frequency components of the flow. In spite of that the vertical spectrum deviates from the prescribed turbulence spectrum, the aerodynamic admittance of both the lift force χ_L and the pitching moment χ_M are in reasonable agreement with Liepmann's approximate solution. The computed admittances χ_L and χ_M are generally 75% higher than the approximation. In the low frequency range the computed admittances deviate below the profile of Eq. (51). This is conjectured to be due to large low frequency turbulent flow structures resulting in instantaneous angles of attack outside the valid range of Eq. (2). For frequencies above 10 rad/s the deviation of the computed admittances to the analytic solution increases further. It is recalled that comparison is performed with the potential flow solution entailing the above-mentioned requirements.

In experiments the aerodynamic admittance has been found to depend on the spectral density of the turbulent fluctuations (Larose and Mann, 1998). When generating the wind tunnel turbulence by spires the measured admittance is generally above Liepmann's approximation (Eq. (51)). However, at the lowest frequencies the measured admittance is considerably below Eq. (51). We believe that the stronger admittance (and in turn the lift signal) is due to body induced turbulence (Larose and Mann, 1998). Both tendencies can be seen at Figs. 11e and f. In the present work the flow around the plate separates due to the turbulent gusts as shown in Fig. 10. Though the ratio of chord to thickness $C/D=12.7$ for the bridge section experiments (Larose and Mann, 1998) is lower than $C/D=200$ for the flat plate, the agreement to of Liepmann's approximation of the thin plate is better for the experimental results. However, the rectangular leading edge of the flat plate used in the present study is blunt, which may increase the aerodynamic admittance as demonstrated experimentally for a $C/D=16$ plate (Larose and Livesey, 1997) cf. Fig. 11e.

5.2.2. Influence of Reynolds number and turbulence intensity

The deviation in the high frequency range of the computed admittances to the analytic solution is suspected to be caused by the viscosity modeling. That is, the standard deviation of the diffusion step length, Eq. (27), influences the magnitude of the high

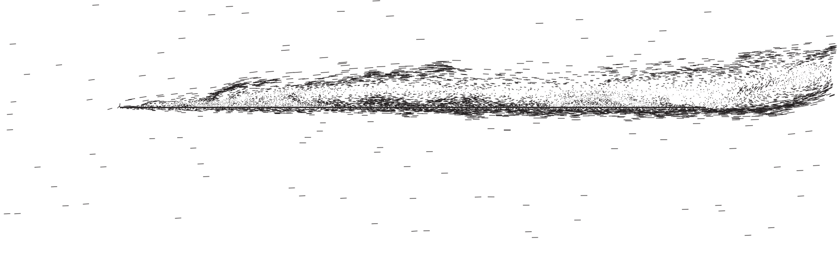

Fig. 10. Flow visualization of turbulent flow past the flat plate at Re=10,000 and I_w=5%. The turbulent fluctuations result in flow separation.

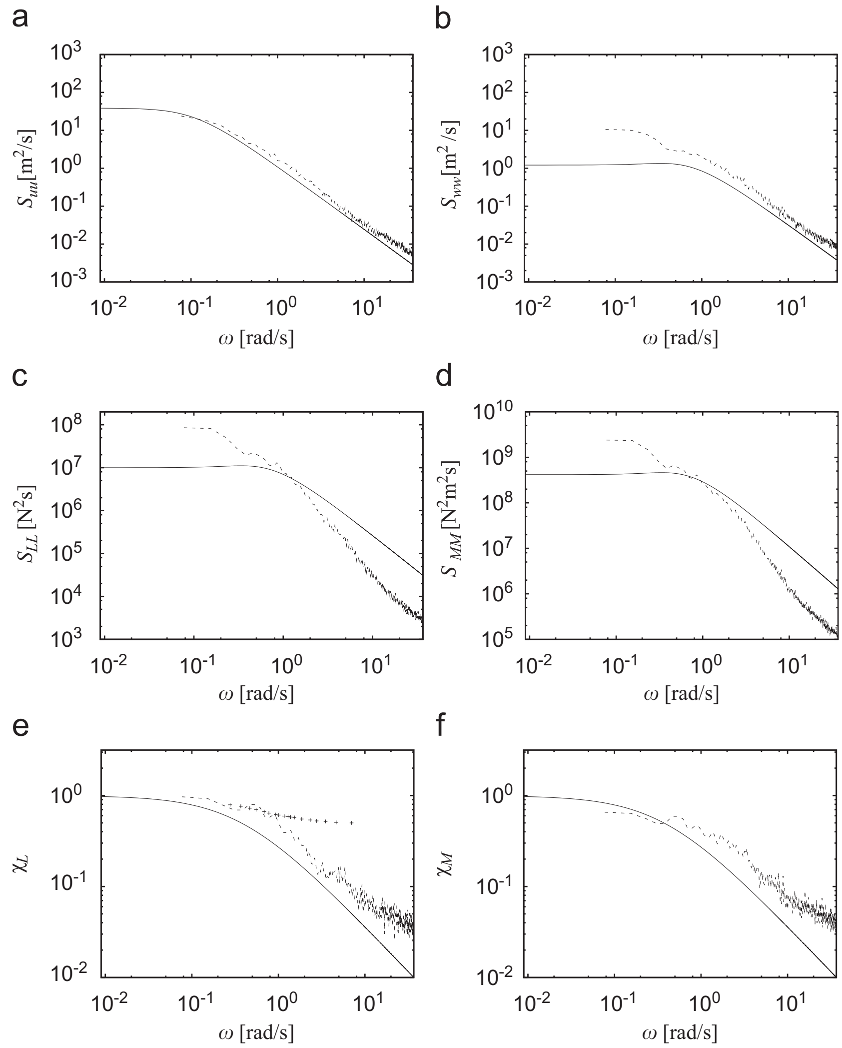

Fig. 11. Spectral densities (- - - - - -) (a) S_{uu} and (b) S_{ww}, and their target (———). (c) S_{LL} and (d) S_{MM} are spectral densities of the lift force and pitching moment (- - - - - -) measured on the flat plate and (———) is the predictions by Eqs. (11) and (12). Aerodynamic admittance of the lift force χ_L (- - - - - -) and experimental results (Larose and Livesey, 1997) for a $C/D=16$ plate (+), (e) and the pitching moment χ_M (f) for the flat plate (- - - - - -), compared to Liepmann's (1952) approximation (———). The graphs are based on 380,000 samples subsampled 100 times. The spectra have been plotted in the range of the discrete frequencies used for turbulence generation.

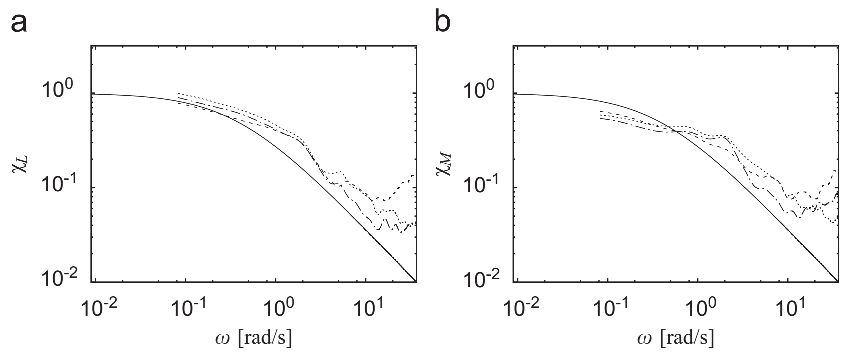

Fig. 12. Aerodynamic admittance of the lift force χ_L (a) and the pitching moment χ_M (b) for the flat plate compared to Liepmann's approximation (———). Results from simulation at Re=1000 (— — — — — —), Re = 10,000 (- - - - - -), Re = 100,000 (—-—-—-). The signals have been subsampled 10 times. The spectra have been plotted in the range of the discrete frequencies used for turbulence generation.

frequency deviation. The reference case is simulated at different Reynolds numbers, by varying viscosity and thereby the average diffusion step lengths. As shown in Fig. 12 the high frequency range of both the lift force admittance χ_L and the pitching moment admittance χ_M decrease with increasing Reynolds number.

As seen in Section 5.1.3 increasing the strength of the particles inserted to generate turbulence increases turbulence intensity. Contrary to expectation the high frequency range deviation is not increased as shown in Fig. 13. The deviation to the analytic solution is decreased considerably and for specified vertical

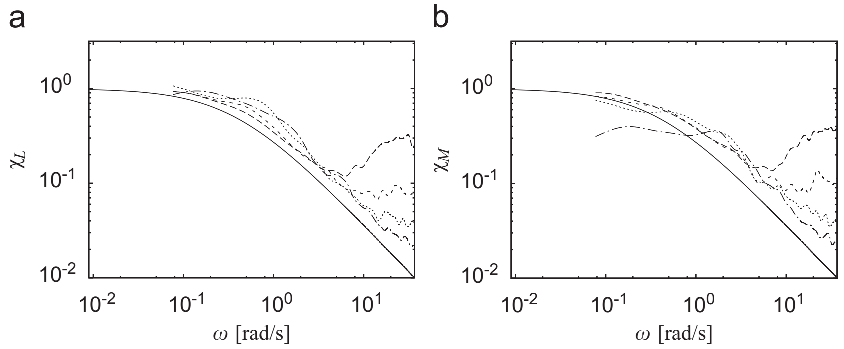

Fig. 13. Aerodynamic admittance of the lift force χ_L (a) and the pitching moment χ_M (b) for the flat plate compared to Liepmann's approximation (———). By varying the specified turbulence intensity from I_w=1.25% (—————), I_w=2.5% (– – – – – –), I_w=5.0% (- - - - - - - - -), I_w=10% (—·—·—·—·) it is seen that the influence from viscous diffusion at the surface becomes less dominant. The signals have been subsampled 10 times. The spectra have been plotted in the range of the discrete frequencies used for turbulence generation.

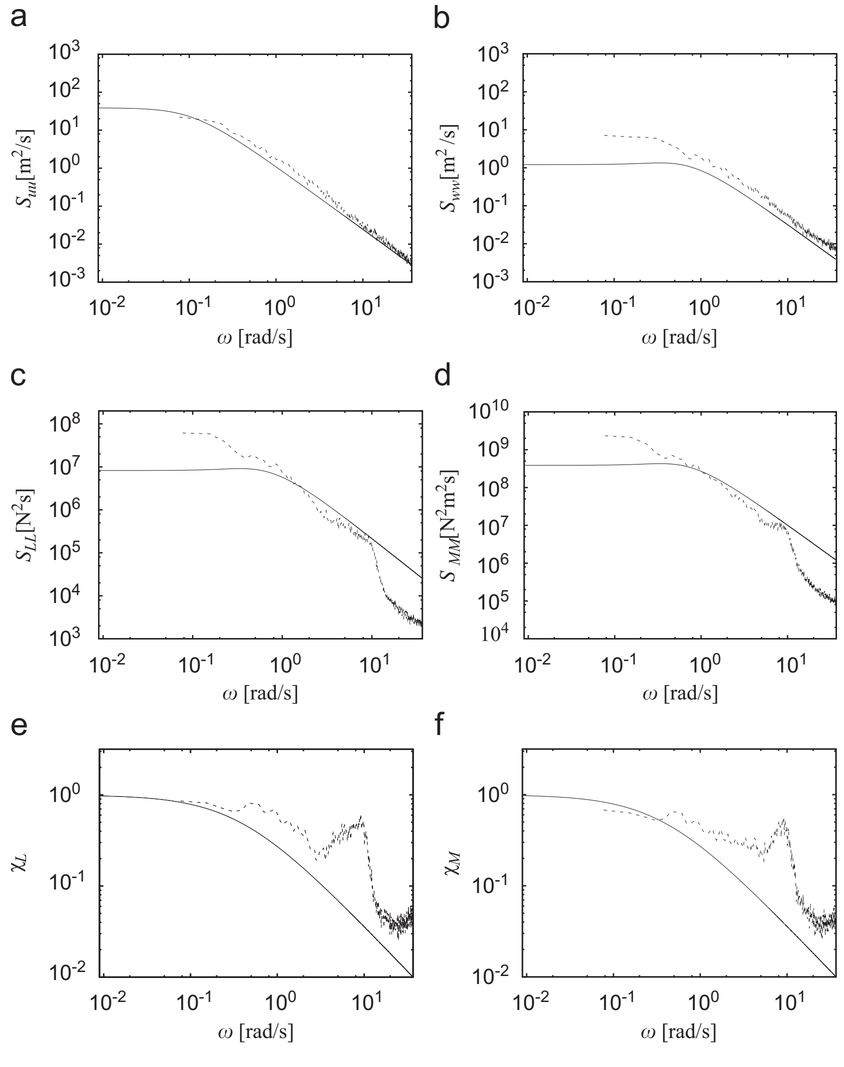

Fig. 14. Spectral density (- - - - - -) (a) S_{uu} and (b) S_{ww}, and their target (———). (c) S_{LL} and (d) S_{MM} are the spectral densities of the lift force and pitching moment (- - - - - -) measured on the Great Belt bridge section and (———) is the predictions by the frequency independent assumption Eqs. (11) and (12). Aerodynamic admittance of the lift force (- - - - - -) χ_L (e) and the pitching moment χ_M (f) for the Great Belt bridge section (- - - - - -), compared to Liepmann's approximation (———). The graphs are based on 380,000 samples subsampled 100 times. The spectra have been plotted in the range of the discrete frequencies used for turbulence generation.

turbulence intensities $I_w \geq 10\%$ the admittance assumes the shape of Eq. (51) from the mid-range frequencies up to ω_{max}. This indicates that the influence of the random walk to the force signal is solely related to the particles generated and emitted from the body surface to enforce the no penetration condition. For bluff bodies, vortex shedding appears in the admittance as a peak at the shedding frequency (not shown). By increasing the turbulence intensity the forces from the turbulent vertical fluctuations become dominant and the admittance tends to the analytic solution (Liepmann, 1952).

5.3. Aerodynamic admittance of Great Belt East bridge section

5.3.1. Comparison with Liepmann

Bridge sections are typically bluff bodies with increased vortex shedding compared to the flat plate. The thickness of the Great Belt East bridge section is $D=0.14C$. Fig. 14 shows the aerodynamic admittance of the lift force χ_L and pitching moment χ_M as well as the corresponding spectral densities. The velocity spectra are equal to those of the flat plate, as shown in Fig. 11. S_{LL} and S_{MM} for the bridge section is of the same order of magnitude as the frequency independent assumption Eqs. (11) and (12) in the frequency interval from 0.8–10 rad/s. This is due to vortex shedding. Therefore using the frequency independent approximation for an initial estimate of the force spectrum may give reasonable results. Outside the interval the agreement is similar to that of the flat plate. Both χ_L and χ_M are stronger than Liepmann's approximation (51) and similar to the admittances of the flat plate. However, the vortex shedding is stronger for the bridge section which manifests itself as a peak in both χ_L and χ_M thereby deviating from the analytic solution that does not take into account vortex shedding. As seen experimentally (Larose and Mann, 1998) the admittance is lower than Eq. (51) at lower frequencies.

6. Conclusions

We have presented a novel technique for the calculation of the aerodynamic admittance in bluff body aerodynamics. The method is based on the two-dimensional discrete vortex method and introduces a turbulent oncoming flow through the insertion of upstream vortex particles modeling the anisotropic turbulent velocity spectra. The admittances of the lift and pitching moment are obtained from the measured spectra of the turbulent flow field and the corresponding spectra of the aerodynamic loads. The method has been validated through detailed simulations of the turbulent flow past a flat plate and past the Great Belt East bridge. The results were found in good agreement with the semi-analytical model of Liepmann and wind tunnel experiments. The method is expected to be a useful engineering tool in bridge aerodynamics.

Acknowledgements

The research has been supported in part by the COWI foundation, and the Danish Research Council (Grant. No. 274-08-0258). Computational resources at the Department of Physics at DTU have been made available through the Danish Center for Scientific Computing (DCSC). The authors wish to acknowledge the collaboration with Sanne Poulin.

Appendix A. ESDU atmospheric turbulence spectra

The Engineering Sciences Data Unit (1993) (ESDU) provides spectral densities of the horizontal and vertical atmospheric turbulent fluctuations, S_{uu} and S_{ww}, respectively. Parameter values used in the present work are stated as the parameters are introduced:

$$\frac{nS_{uu}}{\sigma_u^2}=\beta_1\frac{2.987n_u/\alpha}{[1+(2\pi n_u/\alpha)^2]^{5/6}}+\beta_2\frac{1.294n_u/\alpha}{[1+(\pi n_u/\alpha)^2]^{5/6}}F_1, \tag{52}$$

$$\frac{nS_{ww}}{\sigma_w^2}=\beta_1\frac{2.987[1+(8/3)(4\pi n_w/\alpha)^2](n_w/\alpha)}{[1+(4\pi n_w/\alpha)^2]^{11/6}}+\beta_2\frac{1.294n_w/\alpha}{[1+(2\pi n_w/\alpha)^2]^{5/6}}F_2, \tag{53}$$

with the reduced frequencies

$$n_u=\frac{n(^xL_u)}{U}, \tag{54}$$

$$n_w=\frac{n(^xL_w)}{U}. \tag{55}$$

We use tabulated values of the coefficients α, β_1 and β_2 cf. Harris (1990). In the present work these are $\alpha=0.662$, $\beta_1=0.80$ and $\beta_2=0.20$. The longitudinal standard deviations

$$\sigma_u=\frac{7.5\eta u_*\left[0.538+0.09\ln\left(\frac{z}{z_0}\right)\right]^2}{1+0.156\ln\left(\frac{u_*}{fz_0}\right)}, \tag{56}$$

$$\sigma_w=\sigma_u\left[1-0.45\cos^4\left(\frac{\pi}{2}\frac{z}{h}\right)\right], \tag{57}$$

where

$$\eta=1-\frac{6fz}{u_*}, \tag{58}$$

$$p=\eta^{16}, \tag{59}$$

depend of the friction velocity u_* from the logarithmic law profile

$$U(z)=\frac{u_*}{k}\ln\left(\frac{z}{z_0}\right). \tag{60}$$

k is the von Kármán constant assumed to be 0.4, z_0 is the surface roughness length. u_* is determined from the velocity $U=35$ m/s at $z=70$ m above ground level when $z_0=0.003$ m for open water is used (Engineering Sciences Data Unit, 2001). $f=10^{-4}$ Hz is the mid-latitude Coriolis frequency and $h=660$ m the atmospheric boundary layer thickness. The longitudinal length scales of the horizontal and vertical fluctuations are given by

$$^xL_u=\frac{A_k^{3/2}\left(\frac{\sigma_u}{u_*}\right)^3 z}{2.5K_z^{3/2}(1-\frac{z}{h})^2(1+5.75\frac{z}{h})}, \tag{61}$$

$$^xL_w={}^xL_u\left[0.5\left(\frac{\sigma_w}{\sigma_u}\right)^3\right], \tag{62}$$

and with the present configuration $^xL_u=229.6$ m and $^xL_w=21.8$ m. Also

$$A_k=0.115\left[1+0.315\left(1-\frac{z}{h}\right)^6\right], \tag{63}$$

$$K_z=0.19-(0.19-K_0)\exp\left[-B_k\left(\frac{z}{h}\right)^{N_k}\right], \tag{64}$$

$$K_0=\frac{0.39}{\mathrm{Ro}^{0.11}}, \tag{65}$$

$$B_k=24\,\mathrm{Ro}^{0.155}, \tag{66}$$

$$N_k=1.24\,\mathrm{Ro}^{0.008}, \tag{67}$$

$$\mathrm{Ro}=\frac{u_*}{fz_0}, \tag{68}$$

$$F_1=1+0.455\exp\left[-0.76\left(\frac{n_u}{\alpha}\right)^{-0.8}\right], \tag{69}$$

$$F_2=1+2.88\exp\left[-0.218\left(\frac{n_w}{\alpha}\right)^{-0.9}\right]. \tag{70}$$

References

Alcântara Pereira, L.A., Hirata, M.H., Filho, N.M., 2004. Wake and aerodynamics loads in multiple bodies—application to turbomachinery blade rows. J. Wind Eng. Ind. Aerodyn. 92, 477–491.

Birdsall, C.K., Fuss, D., 1969. Clouds-in-clouds, clouds-in-cells physics for many-body plasma simulation. J. Comput. Phys. 3, 494–511.

Carrier, J., Greengard, L., Rokhlin, V., 1988. A fast adaptive multipole algorithm for particle simulations. SIAM J. Sci. Statist. Comput. 9 (4), 669–686.

Chatelain, P., Curioni, A., Bergdorf, M., Rossinelli, D., Andreoni, W., Koumoutsakos, P., 2008. Billion vortex particle direct numerical simulations of aircraft wakes. Comput. Meth. Appl. Mech. Eng. 197, 1296–1304.

Chorin, A.J., 1973. Numerical study of slightly viscous flow. J. Fluid Mech. 57 (4), 785–796.

Clementson, G.C., 1950. An investigation of the power spectral density of atmospheric turbulence. D.Sc. Thesis, Massachusetts Institute of Technology.

Cottet, G.H., 1990. A particle-grid superposition method for the Navier–Stokes equations. J. Comput. Phys. 89, 301–318.

Davenport, A.G., 1968. The dependence of wind load upon meteorological parameters. In: Proceedings of the International Research Seminar on Wind Effects on Buildings and Structures, pp. 19–82.

Deodatis, G., 1996. Simulation of ergodic multivariate stochastic processes. ASCE J. Eng. Mech. 122 (8), 778–787.

Engineering Sciences Data Unit. Characteristics of atmospheric turbulence near the ground, part ii: single point data for strong winds (neutral atmosphere). Technical Report, 1993.

Engineering Sciences Data Unit. Characteristics of atmospheric turbulence near the ground, part iii: variations in space and time for strong winds (neutral atmosphere). Technical Report, 2001.

Fung, Y.C., 1955. An Introduction to the Theory of Aeroelasticity. John Wiley& Sons.

Ge, Y.J., Xiang, H.F., 2008. Computational models and methods for aerodynamic flutter of long-span bridges. J. Wind Eng. Ind. Aerodyn. 96, 1912–1924.

Greengard, L., Rokhlin, V., 1987. A fast algorithm for particle simulations. J. Comput. Phys. 73, 325–348.

Harris, F.J., 1978. On the use of windows for harmonic analysis with the discrete Fourier transform. Proc. IEEE 66 (1), 51–83.

Harris, R.I., 1990. Some further thoughts on the spectrum of gustiness in strong winds. J. Wind Eng. Ind. Aerodyn. 33, 461–477.

von Kármán, Th., Sears, W.R., 1938. Airfoil theory for non-uniform motion. J. Aerosp. Sci. 5 (10), 379–390.

Koumoutsakos, P., Leonard, A., 1995. High-resolution simulation of the flow around an impulsively started cylinder using vortex methods. J. Fluid Mech. 296, 1–38.

Larose, G.L., 1997. The dynamic action of gusty winds on long-span bridges. Ph.D. Thesis, Department of Civil Engineering, Technical University of Denmark, April.

Larose, G.L., Livesey, F.M., 1997. Performance of streamlined bridge decks in relation to the aerodynamics of a flat plate. J. Wind Eng. Ind. Aerodyn. 71, 851–860.

Larose, G.L., Mann, J., 1998. Gust loading on streamlined bridge decks. J. Fluids Struct. 12, 511–536.

Larsen, A., 1998a. Computer simulation of wind–structure interaction in bridge aerodynamics. Struct. Eng. Int. 8 (2), 105–111.

Larsen, A., 1998b. Advances in aeroelastic analysis of suspension and cable-stayed bridges. J. Wind Eng. Ind. Aerodyn. 74–76, 73–90.

Larsen, A., Walther, J.H., 1997. Aeroelastic analysis of bridge girder sections based on discrete vortex simulations. J. Wind Eng. Ind. Aerodyn. 67–68, 253–265.

Larsen, A., Walther, J.H., 1998. Discrete vortex simulation of flow around five generic bridge deck sections. J. Wind Eng. Ind. Aerodyn. 77–78, 591–602.

Larsen, A., Savave, M., Lafrenière, A., Hui, M.C.H., Larsen, S.V., 2008. Investigation of vortex response of a twin box bridge section at high and low Reynolds numbers. J. Wind Eng. Ind. Aerodyn. 96, 934–944.

Liepmann, H.W., 1952. On the application of statistical concepts to the buffeting problems. J. Aerosp. Sci. 19 (12), 793–800.

Morgenthal, G., Walther, J.H., 2007. An immersed interface method for the vortex-in-cell algorithm. Comput. Struct. 85, 712–726.

Prendergast, J.M., 2007. Simulation of unsteady 2-D wind by a vortex method. Ph.D. Thesis, Department of Engineering, University of Cambridge.

Prendergast, J.M., McRobie, F.A., 2006. Simulation of 2d unsteady wind by a vortex method and application to studying bluff body flow. In: 7th UK Conference on Wind Engineering, pp. 1–4.

Rossi, R., Lazzari, M., Vitaliani, R., 2004. Wind field simulation for structural engineering purposes. Int. J. Numer. Methods Eng. 61 (5), 738–763.

Sbalzarini, I.F., Walther, J.H., Bergdorf, M., Hieber, S.E., Kotsalis, E.M., Koumoutsakos, P., 2006. PPM—a highly efficient parallel particle-mesh library for the simulation of continuum systems. J. Comput. Phys. 215, 566–588.

Shinozuka, M., Jan, C.-M., 1972. Digital simulation of random processes and its applications. J. Sound Vib. 25 (1), 111–128.

Simiu, E., Scanlan, R.H., 1996. Wind Effects on Structures: Fundamentals and Applications to Design. John Wiley & Sons.

Smith, P.A., Stansby, P.K., 1988. Impulsively started flow around a circular cylinder by the vortex method. J. Fluid Mech. 194, 45–77.

Taylor, I.J., Vezza, M., 2001. Application of a discrete vortex method for the analysis of suspension bridge deck sections. Wind Struct. 4 (4), 333–352.

Taylor, I.J., Vezza, M., 2009. A numerical investigation into the aerodynamic characteristics and aeroelastic stability of a footbridge. J. Fluids Struct. 25, 155–177.

Theodorsen, T., 1935. General theory of aerodynamic instability and the mechanism of flutter. TR 496, NACA.

Vejrum, T., Queen, D.J., Larose, G.L., Larsen, A., 2000. Further aerodynamic studies of Lion' gate bridge—3 lane renovation. J. Wind Eng. Ind. Aerodyn. 88, 325–341.

J.H. Walther, 1994. Discrete vortex method for two-dimensional flow past bodies of arbitrary shape undergoing prescribed rotary and translational motion. Ph.D. Thesis, Department of Fluid Mechanics, Technical University of Denmark, September, Unpublished.

Walther, J.H., Larsen, A., 1997. Discrete vortex method for application to bluff body aerodynamics. J. Wind Eng. Ind. Aerodyn. 67–68, 183–193.

Winckelmans, G.S., Leonard, A., 1993. Contribution to vortex particle methods for the computation of three-dimensional incompressible unsteady flows. J. Comput. Phys. 109, 247–273.

Wu, J.C., 1976. Numerical boundary conditions for viscous flow problems. AIAA J. 14 (8), 1042–1049.

Wu, J.C., Gulcat, U., 1981. Separate treatment of attached and detached flow regions in general viscous flows. AIAA J. 19 (1), 20–27.

Zhou, Z., Chen, A., Xiang, H., 2002. Numerical assessment of aerodynamic derivatives and critical windspeed of flutter of bridge decks by discrete vortex method. J. Vib. Eng. 15 (3), 327–331.